Nano Research

Open Access

Research Article

A non-destructive tomographic depth profiling framework for high-precision interface analysis

Zhentao Ma[1,§], Limin Liu[1,§], Xiaokang Liu[1,§], Yide Zhu[1,§], Zixiang Huang[1,2], Mengke Zhang[1], Zirui Xu[1], Wenhao Song[1], Lihui Wu[1], Haibin Pan[1], and Xusheng Zheng[1] ✉

[1] *National Synchrotron Radiation Laboratory (NSRL), University of Science and Technology of China, Hefei 230029, China*
[2] *Hefei National Research Center for Physical Sciences at the Microscale, University of Science and Technology of China, Hefei 230026, China*
[§] *Zhentao Ma, Limin Liu, Xiaokang Liu, and Yide Zhu contributed equally to this work.*

Cite this article: *Nano Research*, **2026**, *19*, 94908486. https://doi.org/10.26599/NR.2026.94908486

ABSTRACT: Non-destructive, depth-resolved characterization is crucial for revealing the evolution of interfacial electronic structures in energy materials and catalytic systems. To overcome the limitations of conventional approaches, which often damage samples and fail to capture true interfacial information, we have established a synchrotron-based platform for non-destructive tomography depth profiling (NDTDP) at the BL10B beamline of Hefei Light Source II. This platform integrates energy- and angle-tunable synchrotron radiation photoelectron spectroscopy with multi-mode soft X-ray absorption spectroscopy, enabling continuous depth profiling from the outermost surface to near-bulk regions. Using single-crystal Si and Cu_2O powders as model systems, we systematically validated the platform's ability to resolve surface oxidation and valence-state gradients, demonstrating high depth resolution and consistency across measurements. These findings establish BL10B as a reliable, NDTDP platform for probing complex interfacial electronic structures and conducting *in situ* studies.

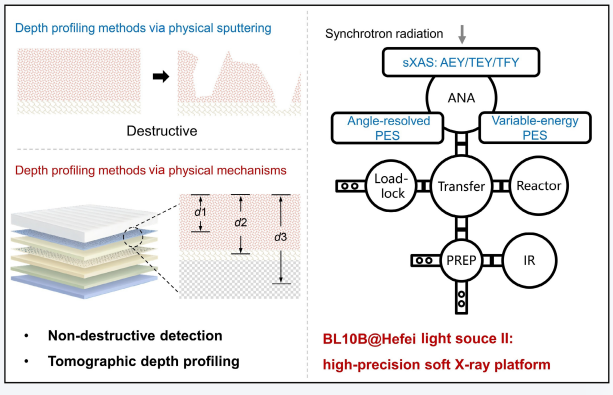

KEYWORDS: BL10B endstation, non-destructive, depth-resolved characterization, interfacial electronic structures

1 Introduction

Interfaces play a critical role in catalysis, energy materials, and functional thin films, where their microscopic structure and chemical state directly govern macroscopic material properties [1–2]. However, conventional characterization techniques struggle to resolve interface information across different depths without causing sample damage. Depth-profiling methods that rely on ion sputtering or mechanical removal, while capable of providing vertical information, inevitably introduce structural modifications or chemical reconstruction, limiting the accuracy of insights into intrinsic interfacial behavior [3–4]. Therefore, developing non-destructive spectroscopic approaches that allow nanoscale control over probing depth is essential to overcome the intrinsic limitations of interface studies.

Received: December 17, 2025; **Revised:** January 19, 2026
Accepted: January 22, 2026

✉Address correspondence to zxs@ustc.edu.cn

Soft X-ray spectroscopy, with its elemental specificity, surface sensitivity, and high spatial resolution, offers unique advantages for probing material surfaces and near-surface regions [5–7]. Following the 2016 upgrade of Hefei Light Source (HLS) to HLS II [8], the photoemission endstation (BL10B) was fully rebuilt to match the new storage ring parameters. The upgraded beamline delivers high-flux soft X-rays ($> 1 \times 10^{10}$ photons/s) over the 100–1000 eV energy range, with soft X-ray absorption spectroscopy (sXAS) energy resolution exceeding 2900 ($E/\Delta E$) and synchrotron radiation photoelectron spectroscopy (SRPES) energy resolution better than 40 meV [9], providing a robust foundation for high-precision, depth-tunable soft X-ray spectroscopy.

Here, we systematically developed a suite of NDTDP soft X-ray techniques employing this enhanced platform. By tuning the incidence angle, photoelectron kinetic energy, and detection mode, these methods enable continuous depth-resolved probing from the extreme surface to near-bulk regions. Using silicon (Si) single crystals and cuprous oxide (Cu_2O) powders as model systems, we validated the approach's ability to resolve surface oxide layers and valence-state gradients, demonstrating both high depth resolution and reproducibility. These results establish BL10B as a reliable

NDTDP platform for nanoscale interface characterization, providing new opportunities to explore interfacial gradients, buried reaction pathways, and surface-bulk coupling mechanisms.

2 Beamline design

The BL10B beamline employs a 1.7 m-long bending magnet with a magnetic field of 1.23 T as the photon source. At a horizontal acceptance angle of 12 mrad, it provides an approximately uniform angular photon flux distribution over the 100–1000 eV energy range, with a source size of roughly 0.29 mm (horizontal, H) × 0.31 mm (vertical, V).

2.1 Beamline design

The beamline is equipped with a self-focusing variable-line-spacing plane-grating monochromator (SF-VLS-PGM) system, as illustrated in Fig. 1. The front-end focusing unit comprises two key optical elements: The first is a vertically mounted cylindrical mirror with a grazing incidence angle of 2.25°, which focuses the horizontal component of the beam between the entrance slit and the plane mirror; the second is a horizontally mounted toroidal mirror at a grazing incidence of 2.5°, which focuses the vertical component of the beam onto the entrance slit, achieving efficient two-dimensional focusing. The monochromator uses a 1400 line/mm plane grating to cover the 100–1000 eV energy range, providing high-resolution monochromatic output across a wide spectral window. The post-focusing system employs a toroidal mirror to simultaneously focus the beam in both horizontal and vertical directions onto the sample position, with a grazing incidence of 2.5°. Key beamline parameters were summarized in Table 1 [9].

2.2 Experimental station

Figure 2 shows the top-view layout and schematic of the experimental station. The system consists of multiple interconnected vacuum chambers to ensure ultra-high vacuum throughout the sample transfer and to enable a variety of preparation and spectroscopic measurement capabilities:

Load-lock chamber: Serves as a transition between atmospheric and ultra-high vacuum, allowing rapid sample loading and unloading.

Table 1 The key parameters of BL10B beamline

Energy range	100–1000 eV
Beam size	1 mm (H) × 1 mm (V)
Flux	> 1×10^{10} photons/s
Resolving power ($E/\Delta E$)	5378@244 eV
Energy repeatability	Better than 0.1 eV@244 eV

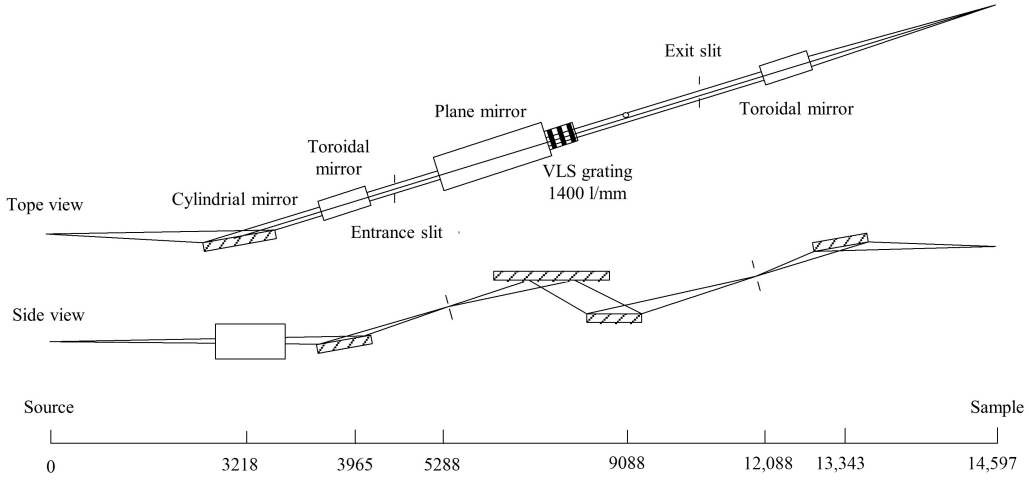

Figure 1 Schematic of BL10B beamline's optical system.

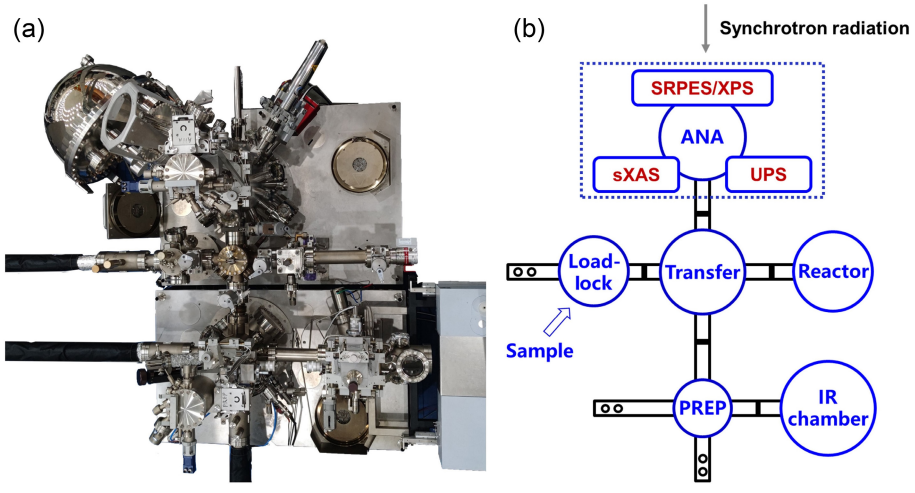

Figure 2 The top-view layout (a) and schematic (b) of the experimental station.

Analysis (ANA) chamber: The core measurement chamber for sXAS, SRPES, and ultraviolet photoelectron spectroscopy (UPS) experiments, directly coupled to the beamline.

Preparation (PREP) chamber: Equipped with an argon (Ar) ion gun and metal evaporation sources for *in situ* surface cleaning and thin-film deposition.

Reactor chamber: Connects to external gas lines, allowing high-temperature and high-pressure treatments under controlled atmospheres without air exposure.

Infrared (IR) chamber: Houses a Bruker VERTEX 80v Fourier transform infrared spectroscopy (FTIR) spectrometer for reflectance and transmission infrared characterization.

Transfer chamber: Functions as a sample transfer node, ensuring efficient and stable movement between functional chambers.

The ANA chamber is fitted with a high-performance electron energy analyzer (Scienta Omicron EW4000, Fig. 3(a) and Fig. S1(a) in the Electronic Supplementary Material (ESM)) with energy resolution better than 5 meV@20 eV, electron acceptance angle ≥ 60°, and a wide working energy range, fully compatible with the beamline. A monochromatic X-ray source (PreVac RMC 50, Fig. 3(b) and Fig. S1(b) in the ESM) provides a small beam spot (< 1 mm × 2 mm), photon flux > 5×10^{10} photons/s, and spectral linewidth < 0.6 eV, serving as a complementary source at higher energies (> 1000 eV) to deepen the probing depth. The four-axis sample manipulator (Fig. 3(c) and Fig. S1(c) in the ESM) allows precise motions along *X*/*Y*/*Z* and rotation about *Z* (*R*), with *X*/*Y* travel of 25 mm (±12.5 mm), *Z* travel up to 400 mm, and *R* rotation ±179°. The manipulator supports a wide temperature range: low temperatures down to 120 K using liquid nitrogen cooling, and high temperatures up to 1200 K via a heating filament embedded in the sample holder, with temperature control precision of ±0.1 K. Such high-precision positioning is crucial for depth-tunable spectroscopic measurements.

The chamber also integrates a custom-built channel electron multiplier (CEM) fluorescence detector, coupled to external picoammeters and current amplifiers, enabling sXAS measurements in both total electron yield (TEY) and total fluorescence yield (TFY) modes. All chambers are constructed from μ-metal for excellent magnetic shielding, suitable for high-sensitivity electron spectroscopy. The vacuum system comprises ion pumps, Ti sublimation pumps, and turbomolecular pumps, achieving a base pressure of 2×10^{-10} mbar after 24 h baking, providing a stable environment for high-quality measurements.

3 Methods

The BL10B beamline at HLS II is a versatile soft X-ray spectroscopy station, integrating three core characterization techniques: sXAS, SRPES/X-ray photoelectron spectroscopy (XPS), and UPS. These techniques collectively probe unoccupied states, core levels, and valence band electronic structures, offering high-sensitivity insight into the electronic states of materials [10, 11].

3.1 sXAS

sXAS is based on the element-specific absorption of X-ray photons by core-level electrons (Fig. 4). When the photon energy matches the excitation energy of a core electron, the electron is excited to an unoccupied state. The resulting core-hole relaxes via spontaneous de-excitation, predominantly through Auger electron emission and fluorescence photon release, with the former generating secondary electron cascades. By tracking the intensity of these de-excitation channels as a function of photon energy, sXAS directly reports the distribution and orbital character of unoccupied states, as well as the local chemical environment and symmetry. As such, it has become a key probe in condensed-matter physics, catalysis, and energy materials research [5, 12–17].

Depending on the detected relaxation signal, sXAS can be performed in electron-yield or fluorescence-yield modes [18, 19]. BL10B implements three modes: Auger electron yield (AEY), TEY, and TFY. TEY measures the total current generated by emitted electrons (including Auger and secondary electrons) using a Keithley 6517A electrometer with resolution from femtoampere to picoampere and low noise. AEY selectively measures emitted Auger electrons via a Scienta Omicron EW4000 energy analyzer, while TFY collects fluorescence photons with a custom-designed channeltron-based detector, transmitting weak signals through vacuum feedthroughs to a current amplifier and computer

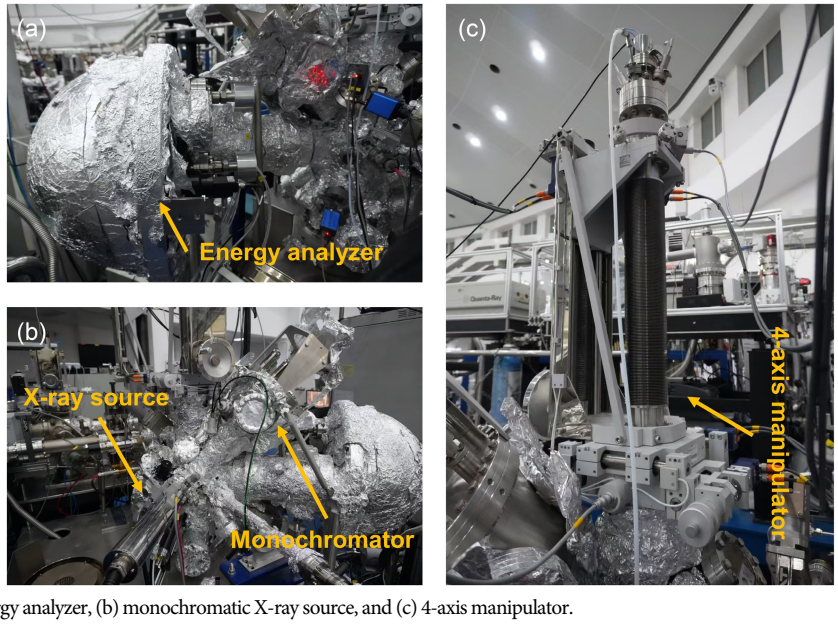

Figure 3 The image of (a) energy analyzer, (b) monochromatic X-ray source, and (c) 4-axis manipulator.

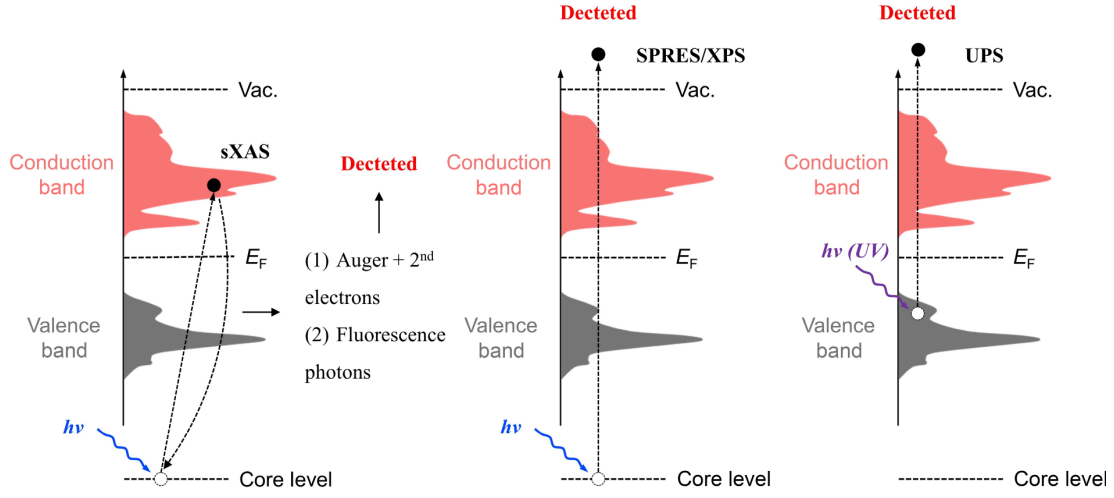

Figure 4 The schematic diagram of sXAS, SRPES/XPS, and UPS.

acquisition. The detector is equipped with two gold meshes at the front and a high-voltage field to suppress stray signals from residual ions and electrons. To compensate for synchrotron flux variations during energy scans, a gold mesh reference is installed upstream of the sample, allowing flux normalization via the measured current. The BL10B beamline provides synchrotron radiation in the energy range of 100–1000 eV, which covers the K-edges of low atomic number elements (e.g., C, N, O), the L-edges of 3d transition metals (e.g., Ti, Fe, Cu), and the M-edges of certain higher atomic number elements (e.g., Ru, Ce) (Fig. S2 in the ESM).

In photochemical studies, sXAS peak intensities correlate with the transition probability of core-to-unoccupied-state transitions. Photoexcitation redistributes electrons between occupied and unoccupied states [20]. Thus, comparing illuminated and dark spectra enables direct identification of photoinduced interfacial charge-transfer processes [21]. For this purpose, the BL10B ANA chamber incorporates a vacuum-compatible optical fiber for *in situ* illumination (200–1200 nm wavelengths, 600 μm core diameter, and up to 1 W power), supporting a wide range of photochemical and photocatalytic measurements.

3.2 SRPES/XPS

Photoelectron spectroscopy (PES, including XPS and SRPES) is a surface-sensitive technique based on the photoelectric effect (Fig. 4). When the photon energy ($h\nu$) exceeds the electron binding energy (E_b), electrons are emitted as photoelectrons, and their kinetic energy (E_k) is used to determine elemental composition and chemical state. Compared with conventional laboratory sources, synchrotron radiation provides high collimation, high monochromaticity, and broad tunability, significantly enhancing spectral precision. With tunable soft X-ray excitation, SRPES can adjust the inelastic mean free path (IMFP) of electrons, enabling depth-resolved measurements from surface-sensitive (< 1 nm) to bulk-sensitive (several nm) regimes [22–24].

At BL10B, emitted photoelectrons are collected and analyzed using a Scienta Omicron EW4000 energy analyzer, with incident photons from 100–1000 eV synchrotron radiation. An additional RMC 50 monochromatic X-ray source (PreVac, Poland; Al Kα 1486.6 eV, Ag Lα 2984.3 eV) provides a complementary high-energy (> 1000 eV) excitation source to enhance spectral quality. This integrated setup enables BL10B to support nearly all elements of photoelectron spectroscopy measurements.

3.3 UPS

UPS is also based on the photoelectric effect but employs low-energy UV photons to excite valence electrons, offering high sensitivity to surface states and low-binding-energy electrons (Fig. 4). UPS measures the valence band energy distribution and secondary electron cutoff, providing critical parameters such as valence band structure, work function, and density of states near the Fermi level, enabling direct insight into the surface electronic properties of materials [25–27].

As for the charging effect, the conductivity requirement at BL10B is mode-dependent: electron-based techniques (AEY, TEY, SRPES/XPS, and especially UPS) require conductive or charge-compensated samples, whereas TFY measurements are essentially free from such constraints.

4 Applications: non-destructive spectro-scopic tomography

The performance of energy materials [28], functional thin films [29], and catalytic systems is strongly shaped by depth-dependent structural gradients and interfacial coupling phenomena [17], including surface reconstruction, subsurface defect modulation, interfacial charge redistribution, and multilayer valence-state evolution. These critical structural motifs are typically buried within the first few to several tens of nanometers and often evolve dynamically under operating conditions. Resolving such buried profiles without damaging the sample is therefore essential for mechanistic understanding and for guiding the design of high-performance devices. However, conventional depth-profiling techniques, such as ion sputtering or mechanical delamination, inevitably perturb the sample and may induce chemical reconstruction, hindering accurate interpretation of intrinsic interfacial behavior (Fig. S3 in the ESM).

To overcome these limitations, we establish an NDTDP approach based on synchrotron soft X-ray techniques. By tuning the effective probing depth through control of photon energy, electron emission angle, or detection channel, this method enables continuous acquisition of electronic-structure and chemical-state information from the extreme surface to the near-bulk region without any physical modification of the sample. This strategy lifts the depth-resolution bottleneck inherent to traditional methods and

is broadly applicable to layered materials, buried reaction interfaces, and functional thin films exhibiting complex vertical gradients.

The BL10B beamline provides the essential experimental infrastructure for implementing this tomography-like capability. High-brightness, energy-tunable soft X-rays allow precise control of photoelectron kinetic energy and thus probing depth, while multiple electron- and fluorescence-yield detection modes greatly expand the accessible information-depth range. Together, these capabilities enable multi-modal, depth-resolved spectroscopic reconstruction of surface, subsurface, and near-bulk regions within a single material system. Notably, the measured spectra represent depth-weighted integrations over different sampling ranges, interpretation of depth-dependent spectral changes should be carried out in conjunction with prior knowledge of the material system and complementary spectroscopic information to avoid overinterpretation (Note S2 in the ESM).

4.1 Depth-resolved PES

In PES, the accessible probing depth is primarily governed by two quantities: the IMFP of electrons in the material and the electron emission angle (θ) relative to the sample surface [30]. The IMFP represents the average distance an electron travels before undergoing inelastic scattering, while the emission angle modulates the effective escape depth through geometric projection. By systematically varying the photon energy and measurement geometry, these parameters form the basis of a non-destructive, continuously tunable, and quantifiable depth-profiling framework, which forms the foundation of our spectroscopic tomography approach.

For a given material, intrinsic properties such as electronic structure and density remain constant. Consequently, the main controllable factor that influences the IMFP is the photoelectron kinetic energy, which is defined by the photoelectric Eq. (1)

$$E_k = h\nu - E_b - \phi \tag{1}$$

where $h\nu$ is the photon energy, E_b is the binding energy, and ϕ is the analyzer work function. Tuning the synchrotron photon energy, therefore, adjusts the E_k and IMFP, enabling depth-selective measurement of core-level spectra.

Several methods exist for estimating IMFP values, including empirical fits to experimental databases, first-principles calculations based on the energy-loss function, and semi-empirical models. The most widely used approach is the Tanuma–Powell–Penn (TPP) family of models, particularly the TPP-2M formulation [31–33]. This model incorporates extensive optical data together with an analytical representation of the Lindhard dielectric function and provides reliable IMFP predictions for most elements and compounds in the 50–2000 eV range. Equations (2)–(7) are the expressions

$$\lambda = E_k / \left\{ E_p^2 \left[\beta \ln(\gamma E_k) - (C/E_k) + (D/E_k^2) \right] \right\} \tag{2}$$

$$\beta = -0.10 + 0.944 \left(E_p^2 + E_g^2 \right)^{-1/2} + 0.069 \rho^{0.1} \tag{3}$$

$$\gamma = 0.191 \rho^{-0.50} \tag{4}$$

$$C = 1.97 - 0.91\, U \tag{5}$$

$$D = 53.4 - 20.8\, U \tag{6}$$

$$U = N_v \rho / M = E_p^2 / 829.4 \tag{7}$$

where λ is the IMFP (in Å), $E_p = 28.8(N_v\rho/M)^{1/2}$ is the free-electron plasmon energy (in eV), ρ is the density (in g/cm^3), N_v is the number of valence electrons per atom (for elements) or molecule (for compounds), M is the atomic or molecular weight, and E_g is the bandgap energy (in eV) for nonconductors.

The second key parameter that governs the probing depth is the electron emission angle relative to the surface normal [34]. In PES, the detected signal from a given depth decays exponentially along the electron's escape path. As a result, the effective information depth scales with the geometric projection of this path and can be expressed as Eq. (8)

$$\lambda_{eff} = \lambda \times \cos\theta \tag{8}$$

where λ_{eff} is the effective inelastic mean free path, and θ is the angle between the photoelectron emission direction and the surface normal of the sample.

By increasing the emission angle toward grazing geometries, the effective escape depth is reduced, and the surface sensitivity is enhanced. This angular dependence provides a powerful and experimentally accessible route to depth tuning, particularly for systems where continuous photon-energy variation is insufficient to isolate subtle depth-dependent features.

To provide a quantitative measure of depth sensitivity, the information depth is commonly defined as the depth from which a chosen fraction (X) of the detected signal originates. Assuming exponential attenuation [35], the corresponding depth is

$$d_X = -\lambda_{eff} \times \cos\theta \times \ln(1 - X) \tag{9}$$

where d_X is the probing depth corresponding to a chosen fraction (X) of the detected signal. The frequently used 95% information depth is approximately

$$d_{95} \approx 3\lambda_{eff} \times \cos\theta \tag{10}$$

and the 99% depth is

$$d_{99} \approx 4.6\lambda_{eff} \times \cos\theta \tag{11}$$

These metrics provide a standardized means of calibrating depth sensitivity in PES.

Although IMFP and θ are the primary factors that determine probing depth, additional effects can also influence the practical information depth. These include elastic scattering, which leads to the effective attenuation length (EAL), as well as surface morphology, interface roughness, charge accumulation, beam incidence angle, and instrumental broadening. Accurate quantitative analysis of depth-resolved PES [35], therefore, requires consideration of sample-specific characteristics and detailed experimental conditions.

4.1.1 *Photon-energy-dependent PES*

To demonstrate the depth-resolving capability based on tunable IMFP, a commercially obtained 10 mm × 10 mm single-crystal Si wafer was first measured using photon-energy-dependent photoelectron spectroscopy. With the electron emission angle fixed at 0°, Si 2p signals were excited using synchrotron soft X-rays at

200, 400, and 600 eV (binding energy range 99–103.3 eV) [36]. According to NIST IMFP experimental data and TPP-2M model calculations, these excitation energies correspond to characteristic probing depths of approximately 1.8 nm (±20%), 3.0 nm (±10%), and 4.2 nm (±10%), respectively. Considering the naturally oxidized surface of commercial silicon wafers, the Si 2p spectra were fitted with two components to distinguish contributions from SiO_2 and intrinsic Si (Fig. 5). The fitting results indicate that under 200 eV excitation, the SiO_2 fraction is approximately 92%; at 400 and 600 eV, the fraction decreases to ~ 70% and ~ 49% (Table 2). As the excitation energy increases and the probing depth deepens, the contribution from the Si substrate correspondingly rises. The observed compositional variation with depth allows estimation of the native oxide layer thickness at ~ 2 nm, consistent with typical natural oxidation behavior of silicon surfaces.

4.1.2 *Angle-dependent PES*

To further demonstrate the control of probing depth via emission angle, angle-dependent photoelectron spectra were acquired on the same Si single crystal with a fixed photon energy of 600 eV, at electron emission angles of 60°, 45°, and 0°. Based on NIST IMFP data and TPP-2M calculations, the 95% information depths for these angles are approximately 2.1 nm (±10%), 3.0 nm (±10%), and 4.2 nm (±10%), respectively. As shown in Fig. 6 and Table 3, at the most grazing angle of 60°, the surface oxide (SiO_2) dominates, accounting for ~ 78% of the signal. As the emission angle decreases to 45°, the SiO_2 contribution drops to 68%, and at normal emission (0°), probing the deepest layer, it further decreases to ~ 50%, with the intrinsic Si signal correspondingly increasing.

Table 2 Depth and SiO_2/Si relative ratio (%) under different synchrotron radiation energies

hv (eV)	Depth (nm)	SiO_2	Si
200	1.8	92.1%	7.9%
400	3.0	70.7%	29.3%
600	4.2	49.3%	50.7%

These angle-dependent results, together with the photon-energy-dependent measurements, demonstrate that both photon energy and emission angle provide independent and quantifiable depth-tuning mechanisms. Continuous probing depths of 1–5 nm can be achieved, and both strategies yield highly consistent estimates of the surface oxide thickness, confirming the self-consistency and reliability of depth-resolved PES. Notably, although both photon-energy-dependent PES and angle-dependent PES approaches enable tunable probing depths, their underlying physical mechanisms differ, which leads to distinct advantages, limitations, and suitable application scenarios in practice. In practical applications, the choice should be made by considering the sample structure, the binding-energy range of the target elements, the specific research objective (e.g., depth evolution of the valence state of a single element versus multi-element compositional profiling), and the surface morphology of the sample (Table S1 in the ESM).

4.2 Depth-resolved sXAS

In sXAS, different de-excitation channels exhibit distinct escape depths. By selecting appropriate detection modes, electronic structure information can be obtained from the extreme surface to near-bulk regions without physical alteration. This characteristic establishes sXAS as a second depth-control method within the non-destructive tomography framework.

For instance, energy-resolved detection of photoemitted electrons using an electron energy analyzer allows selective control of escape depth, typically single atomic layer to 5 nm [37]. Collecting only Auger electrons that have not undergone inelastic scattering limits probing depth to 1–2 nm, giving AEY mode extremely high surface sensitivity. Combining AEY with angle-dependent measurements can achieve atomic-layer-level depth resolution. In contrast, TEY mode collects all emitted electrons, including secondary cascades, resulting in larger effective probing volumes, typically a few nanometers [38]. TFY detected deeper regions due to the much lower scattering and absorption cross-section of photons compared with electrons, enabling near-bulk electronic-structure characterization [39]. By combining AEY, TEY, and TFY data, continuous depth profiles from the surface to bulk

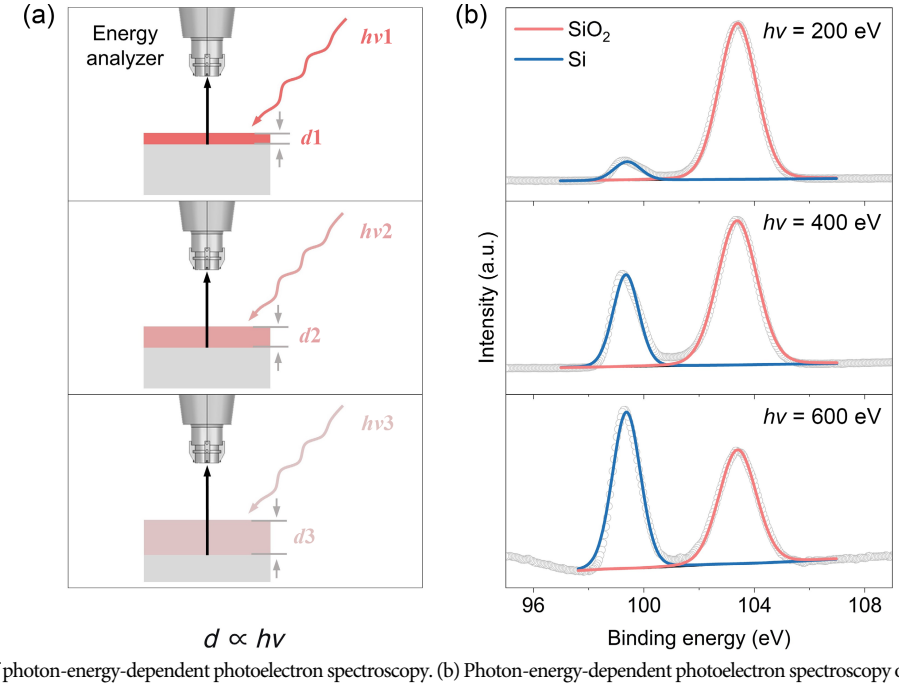

Figure 5 (a) Schematic of photon-energy-dependent photoelectron spectroscopy. (b) Photon-energy-dependent photoelectron spectroscopy of a single-crystal Si wafer.

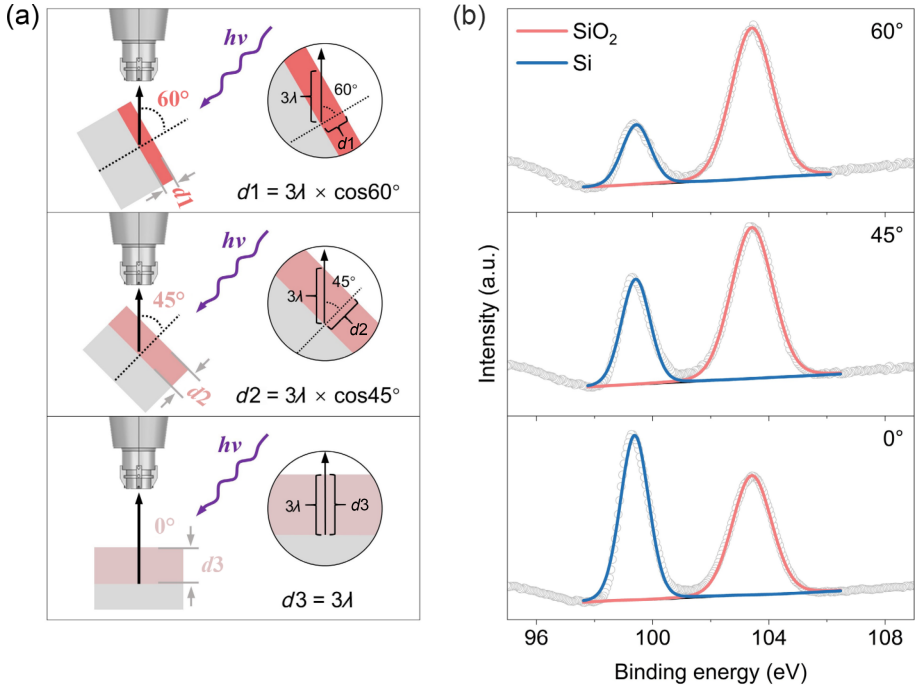

Figure 6 (a) Schematic of angle-dependent photoelectron spectroscopy. (b) Angle-dependent photoelectron spectroscopy of a single-crystal Si wafer.

Table 3 Depth and SiO_2/Si relative ratio (%) under different electron emission angles

θ	Depth (nm)	SiO_2	Si
60°	2.1	78.4%	21.6%
45°	3.0	67.6%	32.4%
0°	4.2	50.2%	49.8%

can be reconstructed, providing non-destructive insight into surface oxidation, interfacial reactions, and multilayer chemical-state gradients.

As an example, Cu L-edge sXAS spectra were measured on commercially obtained Cu_2O powder over the energy range 925–965 eV with a 0.1 eV step. AEY signals were integrated over the $L_3M_{23}M_{45}$ Auger transition. As shown in Fig. 7, the Cu L-edge exhibits strong L_3 and L_2 features at 930–935 and 950–955 eV, corresponding to $2p_{3/2}$ → empty d and $2p_{1/2}$ → empty d transitions, respectively [40]. CuO and Cu_2O show distinct L_3 peaks at 931.2 and 933.9 eV. The Cu(II) ($3d_9$) absorption arises from core-level electrons transitioning to d-hole states. Cu(I), on the other hand, nominally has a filled $3d_{10}$ configuration. Interband transitions are possible due to ds hybridization [41]. The clearly different spectral shapes of CuO and Cu_2O provide reliable fingerprints for identifying their oxidation states [42].

In AEY mode, the Cu^{2+} signal dominates over Cu^+, reflecting the presence of a surface oxide layer. With increasing probing depths, TEY spectra show Cu^+ surpassing Cu^{2+}, while in the deepest probing condition captured by TFY spectra, the Cu^{2+} signal nearly disappears, indicating that the bulk retains the Cu_2O phase (Note S3 in the ESM). This continuous variation from surface CuO to bulk Cu_2O is consistent with typical air-oxidized powder structures, confirming the reliability and sensitivity of depth-resolved sXAS in NDTDP. Notably, the pronounced differences in signal intensities observed among the TFY, TEY, and AEY spectra primarily originate from the distinct physical de-excitation mechanisms following soft X-ray absorption, as well as the intrinsic limitations associated with the signal collection efficiency of each detection mode (Note S4 in the ESM).

Overall, the BL10B beamline uniquely integrates photon-energy-dependent depth tuning, angle-dependent depth control, and multi-channel detection (AEY/TEY/TFY) into a single experimental platform, enabling continuous, non-destructive depth profiling from the extreme surface to the near-bulk region. This system offers superior capabilities for interface analysis relative to other international synchrotron radiation facilities (Table S2 in the ESM).

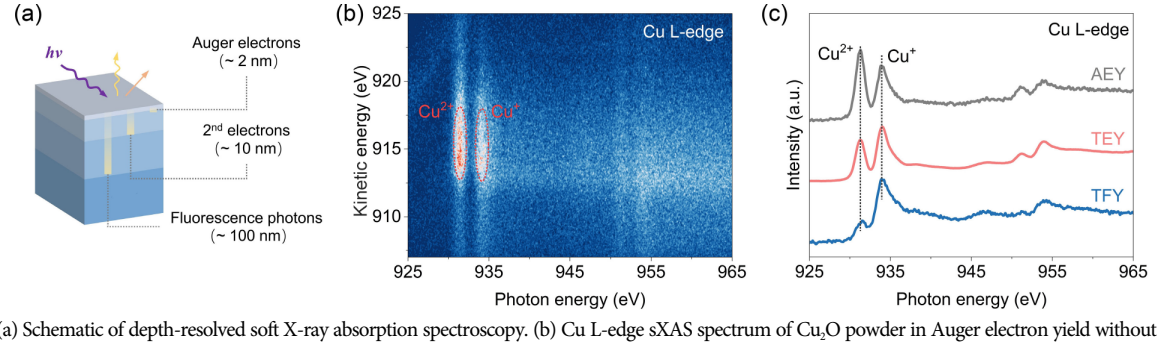

Figure 7 (a) Schematic of depth-resolved soft X-ray absorption spectroscopy. (b) Cu L-edge sXAS spectrum of Cu_2O powder in Auger electron yield without integration. (c) Cu L-edge sXAS spectra of Cu_2O powder in AEY mode, TEY mode, and TFY mode.

5 Conclusions

In summary, a comprehensive NDTDP platform was established at the BL10B beamline of the HLS II. By integrating energy- and angle-tunable SRPES with multi-mode sXAS (AEY/TEY/TFY), continuous depth-resolved analysis from the extreme surface to the near-bulk region was achieved. Experimental validation on single-crystal Si and Cu_2O demonstrates that this approach can reliably resolve surface oxide layers, valence-state gradients, and interfacial chemical environments, yielding results in excellent agreement with the intrinsic material structure. The NDTDP capability of BL10B provides a high-precision platform for *in situ* studies of interfacial electronic structures, energy materials, and catalytic systems under working conditions, and expands the application potential of synchrotron soft X-rays for high-resolution, depth-resolved characterization.

Electronic Supplementary Material: Supplementary material (schematic diagrams of instruments, element coverage of sXAS tests at BL10B, XPS spectra of TiO_2 before and after Ar^+ etching, comparison of photon-energy-dependent PES and angle-dependent PES approaches, and comparison of the depth analysis ability of BL10B with representative soft X-ray beamlines) is available in the online version of this article at https://doi.org/10.26599/NR.2026.94908486.

Data availability

All data needed to support the conclusions in the paper are presented in the manuscript. Additional data related to this paper may be requested from the corresponding author upon request.

Acknowledgements

This work was supported by the National Natural Science Foundation of China (Nos. 12222508, 12475325, and 12205304), the National Key Research and Development Program of China (Nos. 2024YFA1509201 and 2023YFA1506304), Anhui Provincial Natural Science Fundation (No. 2308085MA19), and the Fundamental Research Funds for the Central Universities (No. WK2060250114). The authors thank the beamlines BL10B (31131.02.HLS.PES) in NSRL for synchrotron radiation measurements. This work was partially carried out at Instruments Center for Physical Science, University of Science and Technology of China.

Declaration of competing interest

All the contributing authors report no conflict of interests in this work.

Author contribution statement

Z. T. M.: Conceptualization, methodology, investigation, data curation, formal analysis, writing. L. M. L.: Methodology, visualization, writing. X. K. L.: Conceptualization, writing, funding acquisition. Y. D. Z.: Methodology, investigation, validation, data curation. Z. X. H.: Software, formal analysis, visualization. M. K. Z.: Validation, review. Z. R. X.: Validation, review. W. H. S.: Experimental support. L. H. W.: Resources, technical support. H. B. P.: Conceptualization, review. X. S. Z.: Conceptualization, supervision, funding acquisition, project administration, writing, review & editing.

Use of AI statement

None.

References

[1] Cheng, X. B.; Zhang, R.; Zhao, C. Z.; Wei, F.; Zhang, J. G.; Zhang, Q. A review of solid electrolyte interphases on lithium metal anode. *Adv. Sci.* **2016**, *3*, 1500213.

[2] Ohtomo, A.; Hwang, H. Y. A high-mobility electron gas at the $LaAlO_3/SrTiO_3$ heterointerface. *Nature* **2004**, *427*, 423–426.

[3] Hofmann, S. Sputter depth profiling: Past, present, and future. *Surf. Interface Anal.* **2014**, *46*, 654–662.

[4] Racz, A. S.; Menyhard, M. Evaluation methods for XPS depth profiling; A review. *Appl. Surf. Sci. Adv.* **2025**, *30*, 100872.

[5] Stöhr, J. *NEXAFS Spectroscopy*; Springer: Berlin, 1992.

[6] Wolf, T. J. A.; Myhre, R. H.; Cryan, J. P.; Coriani, S.; Squibb, R. J.; Battistoni, A.; Berrah, N.; Bostedt, C.; Bucksbaum, P.; Coslovich, G. et al. Probing ultrafast ππ*/nπ* internal conversion in organic chromophores via K-edge resonant absorption. *Nat. Commun.* **2017**, *8*, 29.

[7] Wang, Q. Y.; Wan, Y. Y.; Liu, Q. C.; Zhang, Y. D.; Ma, Z. T.; Xu, Z. R.; Sun, P. T.; Wang, G. M.; Jiang, H. L.; Sun, W. P. et al. A multi-site Ru-Cu/CeO_2 photocatalyst for boosting C–N coupling toward urea synthesis. *Sci. Bull.* **2025**, *70*, 1118–1125.

[8] Hu, C. S.; Wang, X.; Qi, Z. M.; Li, C. X. The new infrared beamline at NSRL. *Infrared Phys. Technol.* **2020**, *105*, 103200.

[9] Du, J. J.; Wang, Z. M.; Xu, Z. L.; Pan, H. B.; Wu, L. H.; Zheng, X. S.; Li, C. Y.; Liu, Z. K.; Du, X. W.; Wang, Q. P. Upgrade of the photoemission spectroscopy beamline at HLS-II. *Nucl. Instrum. Methods Phys. Res. Sect. A: Acc., Spectr., Detect. Assoc. Eq.* **2026**, *1082*, 170953.

[10] Zhang, Y. D.; Ma, Z. T.; Yang, S. K.; Wang, Q. Y.; Liu, L. M.; Bai, Y.; Rao, D. W.; Wang, G. M.; Li, H. L.; Zheng, X. S. Element-dependent effects of alkali cations on nitrate reduction to ammonia. *Sci. Bull.* **2024**, *69*, 1100–1108.

[11] Ning, J.; Zhang, B. H.; Siqin, L. T.; Liu, G. H.; Wu, Q.; Xue, S. Q.; Shao, T. T.; Zhang, F. C.; Zhang, W. B.; Liu, X. H. Designing advanced S-scheme CdS QDs/La–Bi_2WO_6 photocatalysts for efficient degradation of RhB. *Exploration* **2023**, *3*, 20230050.

[12] Xu, Q.; Guo, C. X.; Li, B. B.; Zhang, Z. D.; Qiu, Y. J.; Tian, S. B.; Zheng, L. R.; Gu, L.; Yan, W. S.; Wang, D. S. et al. Al^{3+} dopants induced Mg^{2+} vacancies stabilizing single-atom Cu catalyst for efficient free-radical hydrophosphinylation of alkenes. *J. Am. Chem. Soc.* **2022**, *144*, 4321–4326.

[13] Wu, Y. S.; Liu, X. J.; Han, D. D.; Song, X. Y.; Shi, L.; Song, Y.; Niu, S. W.; Xie, Y. F.; Cai, J. Y.; Wu, S. Y. et al. Electron density modulation of $NiCo_2S_4$ nanowires by nitrogen incorporation for highly efficient hydrogen evolution catalysis. *Nat. Commun.* **2018**, *9*, 1425.

[14] Sun, K.; Huang, Y.; Wang, Q. Y.; Zhao, W. D.; Zheng, X. S.; Jiang, J.; Jiang, H. L. Manipulating the spin state of Co sites in metal-organic frameworks for boosting CO_2 photoreduction. *J. Am. Chem. Soc.* **2024**, *146*, 3241–3249.

[15] Zhang, B. X.; Wang, J. M.; Liu, G. M.; Weiss, C. M.; Liu, D. Q.; Chen, Y. P.; Xia, L. X.; Zhou, P.; Gao, M. X.; Liu, Y. F. et al. A strongly coupled Ru–CrO_x cluster-cluster heterostructure for efficient alkaline hydrogen electrocatalysis. *Nat. Catal.* **2024**, *7*, 441–451.

[16] Liu, L. M.; Sun, Y. J.; Ma, Z. T.; Liu, Q. C.; Zhang, R. A.; Wu, L. H.; Pan, H. B.; Wang, Q. Y.; Zhang, Y. D.; Zheng, X. S. Vacancy-induced symmetry breaking in titanium dioxide boosts the photocatalytic hydrogen production from methanol aqueous solution. *Nano Lett.* **2024**, *24*, 13010–13017.

[17] Wang, Q. Y.; Xiao, Y.; Yang, S. K.; Zhang, Y. D.; Wu, L. H.; Pan, H.

B.; Rao, D. W.; Chen, T.; Sun, Z. H.; Wang, G. M. et al. Monitoring electron flow in nickel single-atom catalysts during nitrogen photofixation. *Nano Lett.* **2022**, *22*, 10216–10223.

[18] Wi, S.; Park, J.; Lee, S.; Kang, J.; Hwang, T.; Lee, K. S.; Lee, H. K.; Nam, S.; Kim, C.; Sung, Y. E. et al. Synchrotron-based x-ray absorption spectroscopy for the electronic structure of $Li_xMn_{0.8}Fe_{0.2}PO_4$ mesocrystal in Li^+ batteries. *Nano Energy* **2017**, *31*, 495–503.

[19] Huang, W. F.; Marcelli, A.; Xia, D. G. Application of synchrotron radiation technologies to electrode materials for Li- and Na-ion batteries. *Adv. Energy Mater.* **2017**, *7*, 1700460.

[20] Ma, Z. T.; Wang, Q. Y.; Liu, L. M.; Zhang, R. A.; Liu, Q. C.; Liu, P. G.; Wu, L. H.; Liu, C. Y.; Bai, Y.; Zhang, Y. D. et al. Low-coordination environment design of single Co atoms for efficient CO_2 photoreduction. *Nano Res.* **2024**, *17*, 3745–3751.

[21] Zhao, D. M.; Dong, C. L.; Wang, B.; Chen, C.; Huang, Y. C.; Diao, Z. D.; Li, S. Z.; Guo, L. J.; Shen, S. H. Synergy of dopants and defects in graphitic carbon nitride with exceptionally modulated band structures for efficient photocatalytic oxygen evolution. *Adv. Mater.* **2019**, *31*, 1903545.

[22] Tao, F.; Grass, M. E.; Zhang, Y. W.; Butcher, D. R.; Renzas, J. R.; Liu, Z.; Chung, J. Y.; Mun, B. S.; Salmeron, M.; Somorjai, G. A. Reaction-driven restructuring of Rh-Pd and Pt-Pd core–shell nanoparticles. *Science* **2008**, *322*, 932–934.

[23] Zhang, R. A.; Liu, L. M.; Yang, J. Y.; Xu, Z. R.; Huang, Z. X.; Wu, L. H.; Pan, H. B.; Zheng, X. S.; Gong, M.; Bai, Y. Dynamic restructuring of Pd–Pt concave nanocubes boosts methanol oxidation. *Nano Res.*, **2026**, *19*, 94908165.

[24] Li, L. Y.; Li, Y. X.; Jiao, L.; Liu, X. S.; Ma, Z. T.; Zeng, Y. J.; Zheng, X. S.; Jiang, H. L. Light-induced selective hydrogenation over PdAg nanocages in hollow MOF microenvironment. *J. Am. Chem. Soc.* **2022**, *144*, 17075–17085.

[25] Liu, J.; Liu, Y.; Liu, N. Y.; Han, Y. Z.; Zhang, X.; Huang, H.; Lifshitz, Y.; Lee, S. T.; Zhong, J.; Kang, Z. H. Metal-free efficient photocatalyst for stable visible water splitting via a two-electron pathway. *Science* **2015**, *347*, 970–974.

[26] Xue, J.; Dong, X.; Liu, C. X.; Li, J. W.; Dai, Y. Z.; Xue, W. Q.; Luo, L. H.; Ji, Y.; Zhang, X.; Li, X. et al. Turning copper into an efficient and stable CO evolution catalyst beyond noble metals. *Nat. Commun.* **2024**, *15*, 5998.

[27] Chen, Q.; Huang, J. F.; Chu, D. W.; Cao, L. Y.; Li, X. Y.; Zhao, Y.; Liu, Y. J.; Dong, J. L.; Feng, L. L. Accelerated photogenerated charge separation driven synergistically by the interfacial electric field and work function in Z-scheme Zn-Ni_2P/G-C_3N_4 for efficient photocatalytic hydrogen evolution. *Exploration* **2025**, *5*, 20240189.

[28] Hadouchi, M.; Hou, J. R.; Koketsu, T.; Lahmar, A.; Ma, J. W. Fluorophosphates and fluorosulfates cathode materials: Progress towards high energy density sodium-ion battery. *Nano Res.* **2024**, *17*, 1427–1440.

[29] Meng, Z. A.; Yan, H.; Qin, P. X.; Yin, Z.; Jiang, P. H.; Zhou, X. R.; Wang, X. N.; Chen, H. Y.; Liu, L.; Duan, Z. Y. et al. Emergent ultra-high temperature ferromagnetism in $La_2CoO_{4\pm x}$ thin films. *Nano Res.* **2024**, *17*, 7250–7255.

[30] Krishna, D. N. G.; Philip, J. Review on surface-characterization applications of X-ray photoelectron spectroscopy (XPS): Recent developments and challenges. *Appl. Surf. Sci. Adv.* **2022**, *12*, 100332.

[31] Seah, M. P.; Dench, W. A. Quantitative electron spectroscopy of surfaces: A standard data base for electron inelastic mean free paths in solids. *Surf. Interface Anal.* **1979**, *1*, 2–11.

[32] Tanuma, S.; Powell, C. J.; Penn, D. R. Calculations of electorn inelastic mean free paths. Ⅱ. Data for 27 elements over the 50-2000 eV range. *Surf. Interface Anal*. **1991**, *17*, 911–926.

[33] Tanuma, S.; Powell, C. J.; Penn, D. R. Calculations of electron inelastic mean free paths. V. Data for 14 organic compounds over the 50-2000 eV range. *Surf. Interface Anal*. **1994**, *21*, 165–176.

[34] Hill, M. O.; Kim, J. S.; Muller, M. L.; Phuyal, D.; Taper, S.; Bansal, M.; Becker, M. T.; Bakhit, B.; Maity, T.; Monserrat, B. et al. Depth-resolved X-ray photoelectron spectroscopy evidence of intrinsic polar states in HfO_2-based ferroelectrics. *Adv. Mater.* **2024**, *36*, 2408572.

[35] Powell, C. J. Practical guide for inelastic mean free paths, effective attenuation lengths, mean escape depths, and information depths in X-ray photoelectron spectroscopy. *J. Vac. Sci. Technol. A* **2020**, *38*, 023209.

[36] Seah, M. P.; Spencer, S. J. Ultrathin SiO_2 on Si IV. Intensity measurement in XPS and deduced thickness linearity. *Surf. Interface Anal.* **2003**, *35*, 515–524.

[37] Frazer, B. H.; Gilbert, B.; Sonderegger, B. R.; De Stasio, G. The probing depth of total electron yield in the sub-keV range: TEY-XAS and X-PEEM. *Surf. Sci.* **2003**, *537*, 161–167.

[38] Abbate, M.; Goedkoop, J. B.; de Groot, F. M. F.; Grioni, M.; Fuggle, J. C.; Hofmann, S.; Petersen, H.; Sacchi, M. Probing depth of soft X-ray absorption spectroscopy measured in total-electron-yield mode. *Surf. Interface Anal.* **1992**, *18*, 65–69.

[39] Frati, F.; Hunault, M. O. J. Y.; de Groot, F. M. F. Oxygen K-edge X‑ray absorption spectra. *Chem. Rev.* **2020**, *120*, 4056–4110.

[40] Gurevich, A. B.; Bent, B. E.; Teplyakov, A. V.; Chen, J. G. A NEXAFS investigation of the formation and decomposition of CuO and Cu_2O thin films on Cu(100). *Surf. Sci.* **1999**, *442*, L971–L976.

[41] Ozaslan, D.; Ozkendir, O. M.; Gunes, M.; Ufuktepe, Y.; Gumus, C. Study of the electronic properties of Cu_2O thin films by X-ray absorption spectroscopy. *Optik* **2018**, *157*, 1325–1330.

[42] Zhang, H.; Zhou, J.; Li, X. B.; Han, Y.; Zhang, N.; Liu, Z. Elucidating Raman auger behavior in Cu, Cu_2O and CuO by resonant auger electron spectroscopy to interpret X-ray absorption spectroscopy. *Small Methods* **2025**, *9*, 2402027.